RESEARCH ARTICLE

NANO · MICRO small
www.small-journal.com

Solvent-Free Ball Milling Synthesis of Water-Stable Tin-Based Pseudohalide Perovskites for Photocatalytic CO_2 Reduction

*I-Hua Tsai, Chun-Wei Huang, Chun-Fu Chang, and Eric Wei-Guang Diau**

A pseudohalide (SCN^-) tin-based perovskite material using a solvent-free ball milling method is developed. The synthesized perovskite exhibits long-term water stability and demonstrated significant photocatalytic activity in reducing CO_2 to CO under light irradiation. The structural transition from nanoparticles to planar perovskites is achieved by varying the ratios of dimethylammonium (DMA) and formamidinium (FA) cations, which is confirmed by X-ray diffraction (XRD) and scanning electron microscopy (SEM) analyses. The surface elemental distribution, absorption spectra, band gap and energy levels estimations using energy-dispersive X-ray spectroscopy (EDS), Kubelka-Munk function, and ultraviolet photoelectron spectroscopy (UPS) are thoroughly investigated. These findings indicated that the incorporation of DMA cations increased the band gap and shifted the absorption spectra toward the blue region. The optimal photocatalytic performance is observed for the perovskite composition with a 50% DMA cation ratio ($DMA_{0.5}FA_{0.5}SnI(SCN)_2$), achieving a CO production yield of 285 µmol g^{-1} with 12 hours irradiation in humid environment. The efficiency is critically dependent on the ball milling speed and duration, with 400 rpm and 1 hour being the optimal conditions. This research highlights the potential of environmentally friendly synthesis methods in developing stable and efficient lead-free perovskites as photocatalytic materials, contributing to the goal of net-zero carbon emissions.

1. Introduction

With the rapid development of new technologies, human life has become increasingly convenient. However, this progress has come at the cost of a deteriorating living environment. Since the industrial revolution, human society has relied heavily on the extraction of fossil fuels and thermal power generation, leading to a significant increase in the emission of greenhouse gases such as carbon dioxide (CO_2).[1] The drastic rise in greenhouse gas emissions has exacerbated global warming and extreme climate events, resulting in severe environmental impacts such as polar ice melt causing sea level rise and climate change leading to reduced biodiversity.[2] To mitigate these issues, scientists have been exploring ways to convert atmospheric CO_2 into valuable fuels in addition to reducing the use of fossil fuels.[3] Nature has already evolved the most efficient CO_2 reduction process, photosynthesis, but replicating this process artificially is challenging due to the high bond energy and stability of the C = O bond in CO_2.[4]

Currently, various strategies inspired by natural photosynthesis are being explored, including thermocatalysis,[5] electrocatalysis,[6] and photocatalysis.[7] Among these, photocatalytic reactions, which do not require additional energy inputs, are considered a highly promising strategy. Photocatalytic reactions are photochemical processes that accelerate overall reactions under the influence of a catalyst. Catalysts that can enhance photochemical reactions are known as photocatalysts. The primary function of photocatalysts is to absorb light energy, generate electron-hole pairs, and subsequently initiate a series of chemical reactions.[8] These reactions are typically used to degrade harmful substances, disinfect, and purify air and water. Common photocatalytic materials include titanium dioxide (TiO_2),[9] zinc oxide (ZnO),[10] cadmium chalcogenide (CdS, CdSe, CdTe),[11] and copper oxide (CuO),[12] which are widely studied for their chemical stability, photocatalytic activity, and availability.

Among semiconductor materials, perovskite materials have shown great potential in the field of photocatalysis due to their excellent visible light absorption, simple synthesis

I-H. Tsai, C.-W. Huang, C.-F. Chang, E. W.-G. Diau
Department of Applied Chemistry
Institute of Molecular Science
National Yang Ming Chiao Tung University
1001 Ta-Hseuh Rd., Hsinchu 300093, Taiwan
E-mail: diau@nycu.edu.tw

E. W.-G. Diau
Center for Emergent Functional Matter Science
National Yang Ming Chiao Tung University
1001 Ta-Hseuh Rd., Hsinchu 300093, Taiwan

The ORCID identification number(s) for the author(s) of this article can be found under https://doi.org/10.1002/smll.202409023

DOI: 10.1002/smll.202409023

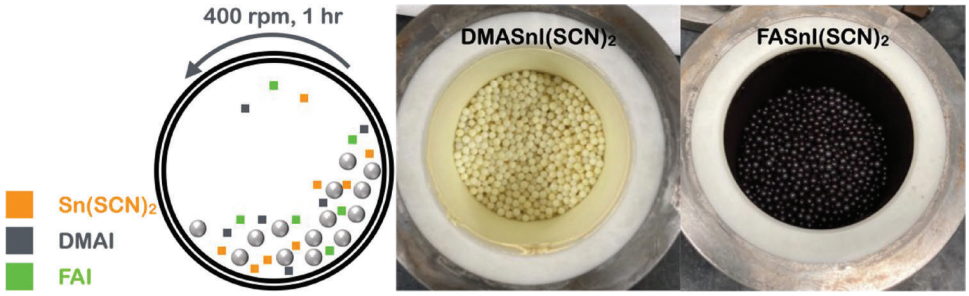

Figure 1. Schematic diagram of the solvent-free ball milling method used for synthesized pseudohalide tin perovskites with varied proportions of A-site cations. The pictures on the right side highlighted the perovskite colors of the synthesized samples, where the $DMASnI(SCN)_2$ (DMA100) sample exhibited a light-yellow color, and the $FASnI(SCN)_2$ (DMA0) sample was characterized by a black color.

methods, suitable energy levels, diverse compositions, and tunable structures.[13,14] Lead-based perovskites have demonstrated outstanding performance in photocatalytic and photovoltaic applications, such as photocatalytic water splitting for hydrogen evolution,[15] CO_2 reduction,[16] and pollutant degradation.[17] However, the stability issues and toxicity of lead pose significant risks in practical applications.[18,19] The environmental and health hazards associated with lead have driven researchers to seek alternative materials, leading to a focus on lead-free perovskites. Therefore, tin is considered one of the most promising alternatives to lead.

Tin-based perovskites, such as $MASnI_3$ and $FASnI_3$, have been extensively studied due to their excellent carrier mobility and high visible light absorption rates, demonstrating significant potential for enhancing photovoltaic conversion efficiencies.[20,21] However, compared to lead perovskites, tin perovskites exhibit poorer stability. Due to the inherent atomic and molecular properties, and the relationship between Gibbs free energy and redox potential, Sn^{2+} has a significantly higher tendency to oxidize than Pb^{2+}. This indicates that under ambient conditions, tin is readily oxidized to Sn^{4+}, leading to the decomposition of tin perovskites and limiting their long-term stability.[22,23] Considering the effective nuclear charge of lead, the relatively weak shielding effect of 4f electrons means that the nucleus of lead exerts a stronger binding force on the outermost 6s electrons (lanthanide shrinkage effect), which contributes to the overall stability of lead-based perovskites.[24,25] To overcome these challenges in tin-based perovskites, scientists have developed strategies involving the substitution of pseudohalides (such as SCN^-) for iodide ions with similar ionic radii, effectively enhancing their stability and moisture resistance while improving the photovoltaic performance of solar cells.[26,27] Furthermore, the hydrophobic organic cation dimethylammonium (DMA) has been utilized for potential environmentally friendly applications in photocatalytic reaction.[28,29] The use of this cation to prepare $DMASnI_3$ perovskite ensures stability in water for up to 16 hours without any degradation.[30] The reversible narrowing of the band gap and the exceptional photovoltaic performance demonstrate that hydrophobic organic cations can indeed effectively help perovskites overcome their drawbacks.

On the other hand, the synthesis methods for perovskites also have varying degrees of impact and harm on the environment. Common synthesis techniques for perovskites include hot injection, ligand-assisted reprecipitation, solvothermal methods, and ultrasonication. Hot injection is a classical and widely used method that allows for the control of photocatalytic performance by altering reaction temperatures, precursor concentrations, and the types and ratios of ligands and precursors.[31,32] Ligand-assisted reprecipitation leverages the solubility characteristics of perovskite precursors, combined with organic ligands, to facilitate perovskite crystallization, enabling straightforward material preparation at room temperature.[33,34] Solvothermal methods employ high temperatures and pressures in a one-pot synthesis approach to produce perovskites with uniform structures and superior performance.[35,36] Ultrasonication uses thermal and vibrational energies to precisely control the dimensions and morphology of the materials, demonstrating the potential of ultrasonication in perovskite synthesis.[37,38] These methods often involve the use of significant amounts of organic solvents, some of which pose potential environmental and health risks, making the reduction of organic solvent use particularly important. To align more closely with the principles of green chemistry, mechanochemical synthesis, including manual grinding[39,40] and mechanical ball milling,[41,42] offers the advantages of minimal organic solvent use and a relatively simple synthesis process. Ball milling achieves similar or even superior yields at lower temperatures and in shorter times, showcasing its energy-efficient and effective characteristics. This method also exhibits significant advantages in controlling particle size and morphology, making it suitable for various applications.

Table 1. Composition of synthesized pseudohalide tin perovskites categorized by the proportion of A-site cations as $DMA_xFA_{1-x}SnI(SCN)_2$.[a)]

Sample	DMAI [mmol]	FAI [mmol]	$Sn(SCN)_2$ [mmol][b)]	DMA content
DMA0	0	3	2	0%
DMA25	0.75	2.25	2	25%
DMA50	1.5	1.5	2	50%
DMA75	2.25	0.75	2	75%
DMA100	3	0	2	100%

[a)] The x value was varied from 0, 0.25, 0.50, 0.75, to 1. The corresponding samples were designated as DMA0, DMA25, DMA50, DMA75, and DMA100, respectively. [b)] It is important to mention that since $Sn(SCN)_2$ is insoluble in water and only deionized water was used for purification in this study, the total amounts of A-site cations were maintained at 1.5 times higher than $Sn(SCN)_2$ to prevent any $Sn(SCN)_2$ remaining in the final product.

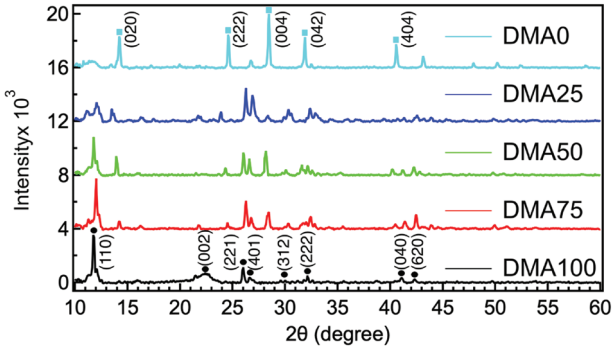

Figure 2. The XRD patterns of the pseudohalide tin perovskites with varied A-site cation ratios. When FA cations were predominant (DMA0), the diffraction signals at 14° and 28° were prominent. In contrast, when DMA cations were predominant (DMA100), the diffraction peaks at 11° and 22° were prominent.

In this study, we developed a DMA-incorporated pseudohalide tin-based perovskite material $DMA_xFA_{1-x}SnI(SCN)_2$ using a solvent-free ball milling method. The perovskite demonstrated long-term stability in water for 24 hours, addressing the stability issue of perovskites, and further showed the capability to photocatalytically reduce CO_2 to CO under light irradiation. For photocatalytic research, employing such environmentally friendly synthesis methods to prepare perovskite materials for carbon dioxide photocatalytic reduction reactions is not only a practice in green chemistry but also an action to minimize carbon footprints in experimental design. This not only meets the stringent environmental protection requirements of modern scientific research but also provides robust technical support for achieving net-zero carbon emission goals.

2. Results and Discussion

Mixed A-site cation (DMA/FA) tin-based pseudohalide perovskites, $DMA_xFA_{1-x}SnI(SCN)_2$, were synthesized following the methods outlined in the experimental section. The synthesis involved adjusting the ratios of DMAI/FAI precursors for $DMA_xFA_{1-x}SnI(SCN)_2$. Detailed schematic diagrams of the synthesis process and the setup for photocatalytic CO_2 reduction experiments were presented in **Figure 1**/**Table 1** and Figure S1 (Supporting Information), respectively. According to the XRD results shown in **Figure 2**, the pseudohalide tin perovskites with primarily FA cations (DMA0, representing as a cyan curve) exhibited prominent characteristic peaks of 3D perovskite at 14° (020) and 28° (004), similar to those observed in $FASnI_3$.[43] As the proportion of DMA cations increased, peaks at lower angles of 11° (110) and 22° (002) gradually appeared and intensified.[44] When the proportion of DMA cation reached 100% (DMA100, representing as a black curve), the peaks at 14° and 28° completely disappeared. This shift in diffraction peaks from higher to lower angles can be explained by Bragg's law, which indicates an inverse relationship between diffraction angles summarized in Table S1 (Supporting Information).[45] Thus, the interplanar spacing (d) of the perovskite lattice increased from 6.2 Å to 7.5 Å with the addition of DMA cations, signifying a structural transition of lattice expansion. Simultaneously, the crystallite size variation was estimated using the Scherrer equation.[46] Without the addition of any DMA cations, the crystallite size was found to be 46.9 nm. However, when the proportion of DMA cations reached 100%, the crystallite size increased to 57.4 nm. This indicated that the incorporation of DMA cations led to lattice expansion, consequently increasing the grain size.

The inclination towards a larger structure upon the addition of DMA cations can be attributed to several factors, primarily the chemical structure of the cations. The DMA cation's molecular formula centers around a nitrogen atom, forming a tetrahedral structure with two methyl groups and two hydrogen atoms bonded via sp^3 hybrid orbitals. In contrast, the FA cation centers around a carbon atom, forming a planar triangular structure with two amino groups and one hydrogen atom bonded via sp^2 hybrid orbitals, with the two amino groups resonating between single and double bonds. Therefore, the larger steric hindrance caused by the two methyl groups of the DMA cation, compared to the planar triangular structure of the FA cation. Besides, the lower bond order of the DMA cation's C—N bond compared to the resonating C—N bond in the FA cation, result in a slightly larger effective ionic radius for the DMA cation (2.72 Å) compared to the FA cation (2.53 Å).[47] Consequently, the perovskite lattice expands to accommodate the larger DMA cations.

The Goldschmidt tolerance factor (t) was used to estimate the impact of DMA cations on the BX_6 octahedra shown in Table S2 (Supporting Information).[48,49] When DMA was not added (DMA0), t was 1.00. With the incorporation of DMA cations to 100%, t increased to 1.04. Although previous studies have indicated that the ideal cubic structure of perovskites has a t value in the range of 0.9-1.0, and larger cations typically lead to higher t values, the primary reason for using DMA cations in this study was to enhance the water stability of the perovskite. The difference in the effective radius between the two cations, FA and DMA, was not only due to their steric structures but also influenced by the location of their positive charges, which affects the stability of the perovskite. For instance, in FA, the positive charge is located on the outer nitrogen atom, making it more susceptible to nucleophilic attack by water molecules from the environment, leading to perovskite degradation. In contrast, the positive charge in DMA is positioned on the carbon atom at the center, protected by two methyl groups, making it more resistant to such attacks. Therefore, although the tolerance factor might suggest that the structural stability of the perovskite in this study is not as robust as that of commonly known perovskites like $FASnI_3$ (t = 1.00) or $MASnI_3$ (t = 0.92), the hydrophobic nature of the molecular structure involving DMA cation was a key consideration.[50] The steric hindrance and the centrally located charge of DMA cations contribute to improved water stability. This trade-off between structural tolerance and environmental stability suggests that A-site organic molecules with similar characteristics to DMA, having steric hindrance groups and centrally located charges, should be considered in the future for the preparation of water-stable perovskite materials. In molecular design considerations, it is crucial to select cations that not only possess hydrophobic functional groups but also feature a molecular geometry that introduces steric hindrance. Additionally, positioning the positive charge centrally within the molecule helps in minimizing interactions with water molecules. Therefore, future

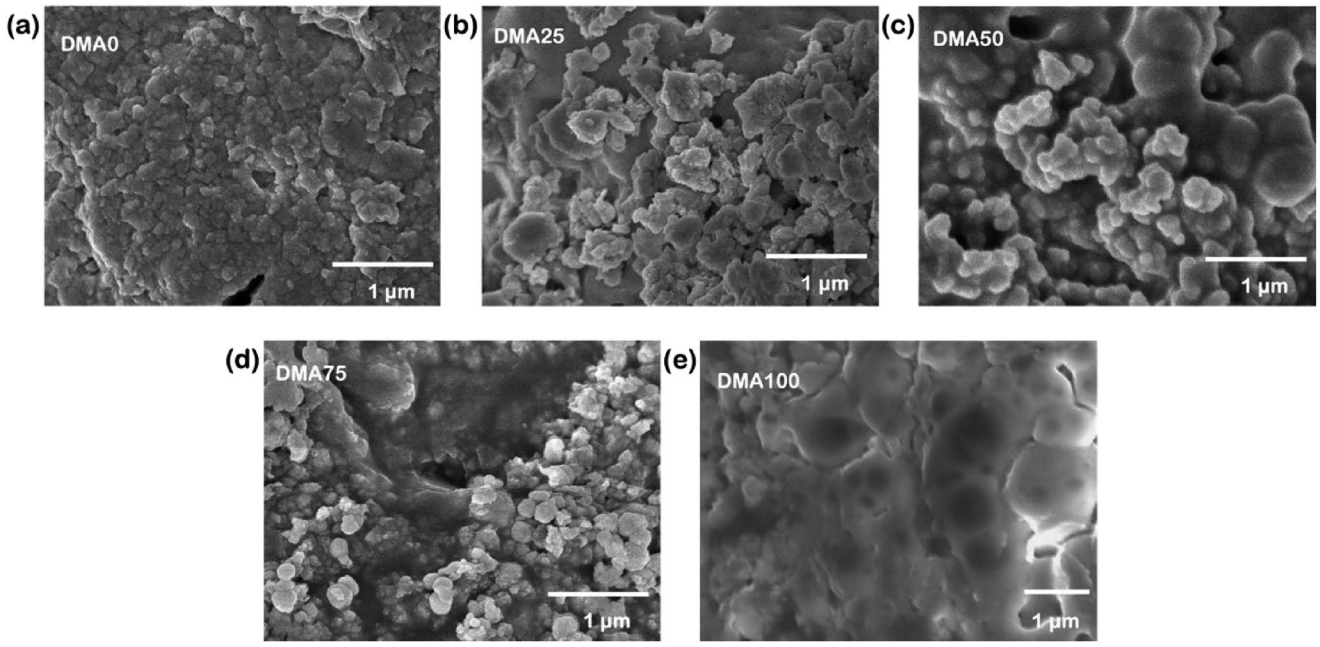

Figure 3. High-magnification SEM images of pseudohalide tin perovskites prepared by solvent-free ball milling for a) DMA0, b) DMA25, c) DMA50, d) DMA75 and e) DMA100.

perovskite molecular designs should incorporate these characteristics to achieve water-stable photocatalytic materials.

Moreover, the XRD peak shift observed in this study differs from the commonly reported 2D perovskite types, such as Ruddlesden-Popper (RP)[51] and Dion–Jacobson (DJ)[52] perovskites. In RP or DJ type perovskites, the cations used typically possess long carbon chain structures, and as the number of perovskite lattice layers (n) decreases, the XRD peak position gradually shifts to lower angles. However, in this study, when 25% DMA cations were incorporated, their diffraction peaks appeared directly at specific diffraction angles. This indicates that the DMA cations were co-incorporated with FA cations into the sub-lattice, rather than acting as spacers to form a 2D perovskite structure. Comparative analysis of the XRD patterns of DMA cation or pseudohalide tin perovskites synthesized using different methods revealed that the perovskites synthesized by Rameez et al. using a two-step annealing method and those synthesized by Tao's research group using an acid precipitation method were both characterized as $FASnI(SCN)_2$ and $DMASnI_3$, respectively.[27,44] In our case, the similarity with their XRD diffraction peaks confirmed the viability of synthesizing pseudohalide tin perovskites using a solvent-free ball milling method.

Based on SEM images in Figure S2 (Supporting Information), the morphology of the perovskite without any DMA cation addition displayed a uniform distribution of nanoparticles. As the proportion of DMA cations increased to 100%, these spherical structures disappeared and transformed into smooth planar structures. To more clearly observe the transition induced by DMA cations, SEM images were obtained (**Figure 3**) for samples with DMA0, DMA25, DMA50, DMA75, and DMA100. It was found that the addition of DMA cations resulted in a coexistence of nanocrystals and multilayered structures. Notably, in the DMA50 sample, the particle structures were observed to be embedded within the planar structures. The transformation from spherical nanoparticles to smooth planar structures indicates a significant reorganization of the material's internal lattice, likely due to the unique role of DMA cations in promoting lattice expansion and structural rearrangement. This observation is critical as it highlights the potential of DMA cations in tailoring the morphology and structural properties of perovskites, which could be leveraged to optimize their performance in various applications such as photocatalysis and optoelectronic devices. These findings successfully demonstrate that through the solvent-free ball milling method, perovskite structures with nanoparticle sizes ranging from approximately 1 μm to 100 nm can be transformed into flat, planar structures. The morphological evolution observed with increasing DMA cation content suggests that DMA not only affects the size and shape of the crystallites but also influences the overall structural organization of the perovskite material. Therefore, the solvent-free ball milling method proved to be an effective approach for inducing these transformations, offering a pathway to finely tune the physical properties of perovskites through controlled cation incorporation.

Further SEM-EDS analysis was conducted to examine the elemental composition and distribution on the surface of the perovskite, with a focus on the elemental ratios in DMA50. Figure S3 (Supporting Information) shows the SEM image of the EDS measurement location (DMA50) and the energy peaks of each element. The statistical analysis of these energy peaks is summarized in Table S3 (Supporting Information), revealing the elemental ratios of C, N, S, Sn, and I as 38.14%, 43.15%, 6.62%, 8.79%, and 3.30%, respectively. The relatively high atomic percentages of C and N indicated that the perovskite surface was predominantly modified by DMA cations, resulting in lower proportions of Sn, S, and I, thus deviating from the precursor

stoichiometric ratios. Moreover, elemental mapping images in Figure S4 (Supporting Information) demonstrated that all elements were uniformly distributed throughout the perovskite, with the combined image showing a high degree of overlap.

These findings suggest that the incorporation of DMA cations significantly altered the surface chemistry of the perovskite. The elevated levels of carbon and nitrogen are consistent with the presence of DMA cations, which likely dominate the surface due to their high surface energy and strong interaction with the perovskite. This surface modification not only influences the elemental distribution but also impacts the overall stability and performance of the perovskite material. The uniform distribution of elements, as evidenced by the elemental mapping, indicates a homogeneous modification process, which is crucial for maintaining the integrity and functionality of the perovskite structure. Such a homogeneous distribution could enhance the material's photoactive properties by providing a consistent interface for charge transport and reducing defect sites that could act as recombination centers. This uniformity is particularly important for applications in photovoltaics and photocatalysis, where surface composition and homogeneity directly affect their efficiency and stability.

To understand the absorbance of various pseudohalide tin perovskites at different wavelengths and estimate their band gaps (E_g), the absorption spectra were measured. However, since the perovskites synthesized by solvent-free ball milling method were in powder form, preparing them as thin films for absorption measurements was challenging due to their opacity and the need to account for surface scattering and roughness. Consequently, we pressed the samples into 2 mm thick pellets and measured their reflectance spectra using an integrating sphere. The Kubelka-Munk function was then employed to approximate the absorption spectra.[53] As shown in Figure S5a (Supporting Information), the absorption signal of DMA0 spanned almost the entire visible light region, which correlated with the black powder observed in the samples. With the incorporation of DMA cations, the sample color gradually shifted to light yellow, and the absorption signal in the 500–800 nm wavelength range weakened. This absorption signal weakened could be attributed to transitions caused by the surface defects passivation with DMA cations in the perovskite nanocrystals. As the proportion of DMA cations increased, the defect-related absorption signals decreased, indicating that the surface defects were being passivated by the DMA cations. This observation was consistent with the SEM and EDS results.

We further calculated the band gaps of the tin perovskites samples (DMA0, DMA25, DMA50, DMA75, and DMA100) using the $(F_R h\nu)^2$ function, following the Tauc plot method to approximate the band gaps, as shown in Figure S5b (Supporting Information). The estimation involved fitting two linear trend lines and finding their intersection point. The first trend line was fitted from 1.1 eV to 1.5 eV as a baseline. The second trend line was determined by finding the position of the maximum slope using a differential equation and fitting a linear function to this region. The intersection of these two lines provided the band gap values for DMA0 (E_g = 2.49 eV), DMA25 (E_g = 2.68 eV), DMA50 (E_g = 2.74 eV), DMA75 (E_g = 2.74 eV), and DMA100 (E_g = 2.79 eV). These results indicated that the addition of DMA cations led to a blue shift, suggesting that the incorporation of DMA cations widened the band gap. The widening of the band gap with increasing DMA content can be attributed to the alteration in the electronic structure of the perovskite. The DMA cations, due to their larger size and unique electronic properties, likely introduced new energy levels or modified existing ones, leading to the observed changes in the band gap. The decrease in defect-related absorption with increasing DMA content also implies an improvement in the material's structural integrity and stability. Surface defects in perovskites are known to act as non-radiative recombination centers, which can significantly reduce the efficiency of photovoltaic devices.[54] By passivating these defects, DMA cations enhance the material's photophysical properties, potentially leading to a better performance in practical applications.

The changes in band gaps can be hypothesized based on a simple molecular orbital (MO) theory model.[55] As illustrated in Figure S6 (Supporting Information), the metal ions at the B-site utilize ns and np orbitals, while the anions at the X-site employ np orbitals for MO hybridization. When the A-site cation is small, such as the FA cation (with an effective radius of 2.53 Å), the band gap is as shown in the Figure S6a (Supporting Information). However, the incorporation of larger cations, such as the DMA cation (with an effective radius of 2.72 Å), leads to lattice expansion. This expansion weakens the bonding strength of the B-X bonds. As the bonding strength decreases, the interaction between the ns orbital of the B-site metal and the np orbital of the X-site anion reduces, resulting in a lower valence band maximum, conduction band minimum and consequently a wider band gap. Another perspective on the widening band gap considers the quantum confinement effect.[56] When the size of the A-site cation in the perovskite lattice is too large, the BX_6 octahedra cannot maintain the 3D lattice structure. The lattice then segregates along the direction of the cation, forming a 2D perovskite, similar to the RP type and DJ type 2D perovskites previously mentioned. In this scenario, the A-site cation creates a natural quantum well (QW) confinement structure. The enhanced confinement effect causes the valence band position to shift downward while the conduction band position shifts upward, leading to a wider band gap and a noticeable blue shift in the absorption spectrum. According to the XRD spectral results, the perovskite in this study did not exhibit characteristics of RP type or DJ type 2D perovskites. Therefore, the applicable molecular orbital model should account for the widening band gap due to the 3D perovskite structure with large A-site cations.

To verify the accuracy of the aforementioned model, the work function and valence band maximum of the pseudohalide tin perovskite materials were measured to confirm their energy level positions. Ultraviolet photoelectron spectroscopy (UPS) effectively provided this information. The estimated values for all samples were determined using the intersection of the two linear functions. First, the cut-off energy ($E_{cut\text{-}off}$) was obtained by linearly fitting the baseline trend line (20 eV – 17 eV) for each sample and using a differential equation to acquire the differential extremum's linear function trend line. The intersection of these two lines determined the cut-off energy. The binding energy (E_b) was based on the linear fit of the baseline trend line (−1 eV – 0 eV) and the linear fit of the trend line in the region where the signal intensity was 1%. As shown in Figure S7 (Supporting Information), calculations were performed based on the law of energy conservation, where the total energy of the incident light source ($h\nu$) was

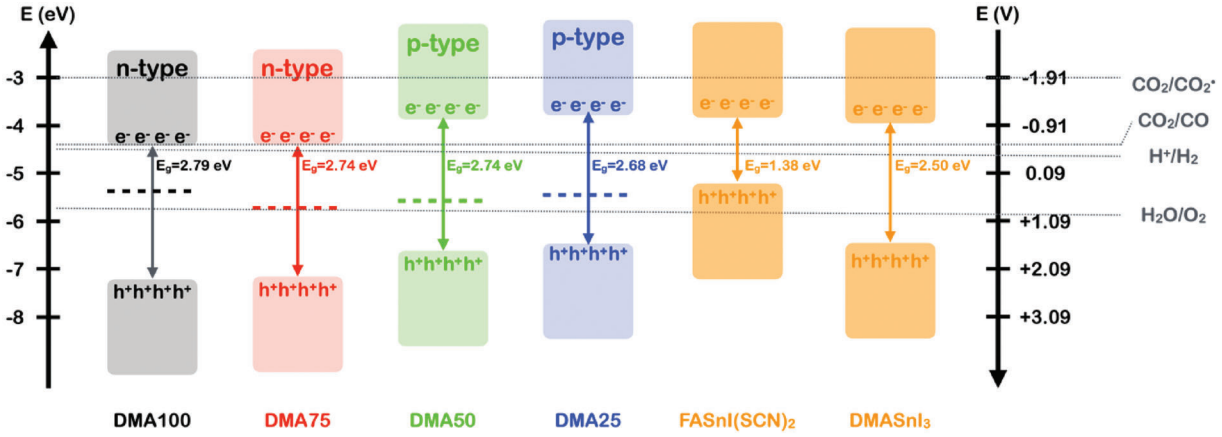

Figure 4. Redox energy level diagram of pseudohalide tin perovskites prepared by solvent-free ball milling. The energy levels of $FASnI(SCN)_2$ and $DMASnI_3$ are adopted from previous studies.[27,44]

21.22 eV. The work function (Φ) was calculated as $\Phi = h\nu - E_{cut\text{-}off}$, and the valence band maximum (VBM) was calculated as VBM $= \Phi + E_b$. Therefore, the work functions of perovskites with varying DMA cation incorporation ratios (DMA25, DMA50, DMA75 and DMA100) were 5.6 eV, 5.6 eV, 5.7 eV, and 5.4 eV, and the valence band maxima were 6.5 eV, 6.6 eV, 7.2 eV, and 7.2 eV, respectively. From these results, it was observed that although the work function of the perovskites did not exhibit significant variations with increasing DMA cation incorporation, the valence band position decreased as the proportion of DMA cations increased. The slight variations in the work function observed among the different DMA incorporation ratios suggest that the surface electronic environment of the perovskite materials was moderately influenced by the DMA cations. However, the more pronounced shifts in the valence band maximum indicate a significant impact on the bulk electronic structure. This experimental outcome was consistent with the previously proposed model for changes in the band gap and valence band position.

Further, a comprehensive energy level diagram was constructed by plotting the work function, valence band maximum, and band gap, summarized in Table S4 (Supporting Information). The diagram also marked the reduction potential of CO_2 to CO and the oxidation potential of H_2O to O_2, as shown in **Figure 4**. These parameters are crucial for understanding the suitability of these materials for photocatalytic applications, where the alignment of energy levels with the redox potentials of target reactions is essential. Based on the energy level diagram, it was observed that all pseudohalide tin perovskites possessed reduction potentials suitable for photocatalytic CO_2 reduction. Notably, the reduction potentials of DMA25 and DMA50 were significantly higher than that of CO_2/CO, while those of DMA75 and DMA100 were only slightly higher by approximately 0.03 eV. The higher reduction potentials observed for DMA25 and DMA50 than for DMA75 and DMA100 suggest a stronger driving force for electron transfer processes, which are essential for effective photocatalytic activity. In contrast, the marginally lower reduction potentials of DMA75 and DMA100, while still adequate for CO_2 reduction, indicated a nuanced control over the electronic properties with increasing DMA content. Furthermore, an interesting phenomenon was noted: as the incorporation ratio of DMA cations increased, the semiconductor type of the perovskite materials transitioned from p-type to n-type. The incorporation of DMA cations likely introduced new electronic states or modified existing ones, leading to a reorganization of the energy levels and a shift in the Fermi level. This indicated that the DMA cations played a crucial role in reorganizing and altering the electronic structure of the pseudohalide tin perovskites.

Based on the aforementioned characterizations, all perovskites demonstrated the potential to absorb visible light for photocatalytic CO_2 reduction. The individual photocatalytic efficiencies were shown in **Figure 5a**. When no DMA cations were incorporated into the perovskite structure (DMA0), the sample exhibited negligible catalytic efficiency. However, with the incorporation of 25% DMA cations (DMA25), the CO production efficiency rapidly increased to 166 μmol g^{-1} in 12 hours. This result suggests that in the absence of DMA cations, the perovskite structure was susceptible to degradation by water vapor, leading to naught photocatalytic efficiency. In contrast, the addition of 25% DMA cations significantly protected the perovskite structure. Increasing the DMA cation ratio to 50% further enhanced the CO production yield to 285 μmol g^{-1} in 12 hours. However, further increases in the DMA cation ratio led to a decline in photocatalytic efficiency. This decrease correlated with changes in the reduction potential; the reduction potentials of DMA75 and DMA100 were only slightly higher than the energy level of the CO_2/CO redox. If charge carriers were affected by intrinsic defects in the material, reducing their electrochemical potential (i.e., redox capability), they could not effectively participate in the photocatalytic reaction, resulting in diminished efficiency. Moreover, as the DMA cations fully replaced the FA cations, the bandgap widened, reducing the effective solar spectrum region available for photocatalysis and lowering the charge carrier density.

Among the different cation ratios tested, DMA50 exhibited the best photocatalytic performance. To further optimize the solvent-free ball milling process, the milling speed was varied at 100 rpm, 200 rpm, 300 rpm, 400 rpm, and 500 rpm for 1 hour (Figure 5b). The CO production rates were 22, 115, 181, 285, and 68 μmol g^{-1} in 12 hours, respectively. These results indicated that the milling speed critically influenced the perovskite yield, with 400 rpm achieving the highest CO production yield. However, the

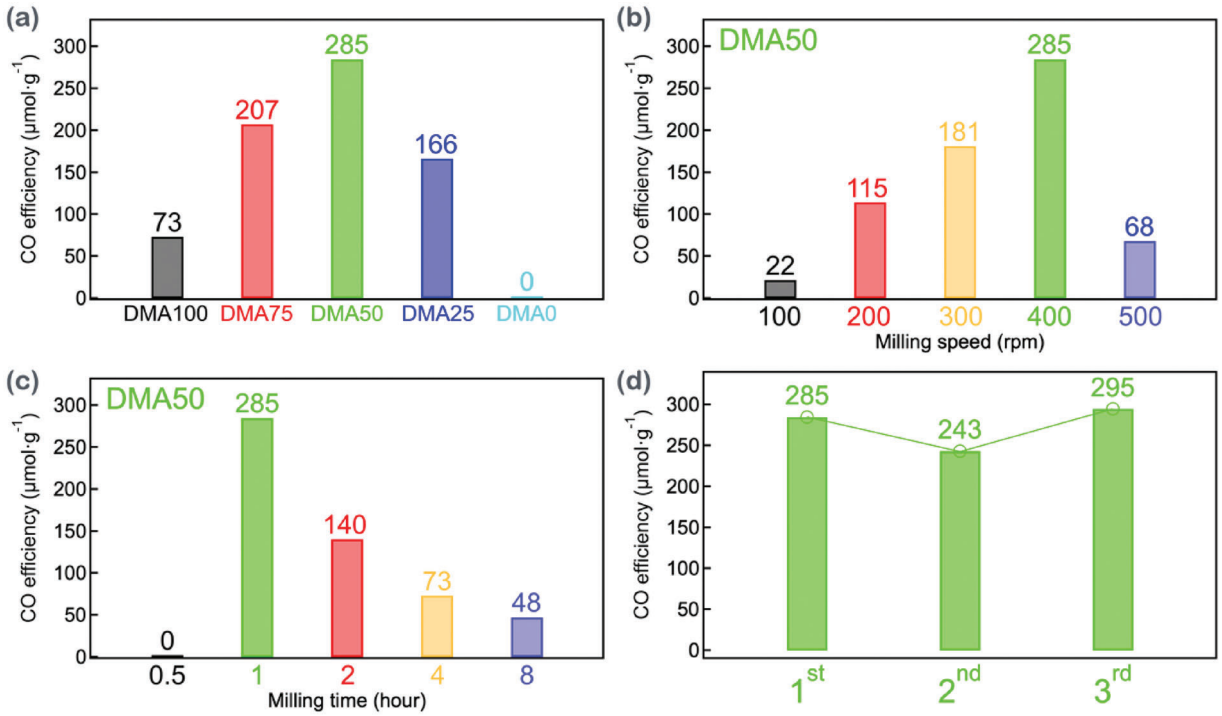

Figure 5. CO production yields from CO_2 photoreduction in 12 hours. a) Different cations ratios, b) DMA50 at varied ball milling speeds, c) DMA50 at different ball milling durations, and d) reproducibility of DMA50 for repeating the experiments for three times.

photocatalytic efficiency sharply decreased at 500 rpm, likely due to heat generation during milling, which caused perovskite degradation. Since no solvent or external temperature control was used in this study, the heat generated during milling could not be dissipated, suggesting a future research direction to mitigate heat interference. Another crucial parameter in the ball milling process was the milling time, which also significantly affected the perovskite yield. Milling time of 0.5, 1, 2, 4, and 8 hours resulted in CO production rates of 0, 285, 140, 73, and 48 μmol g^{-1} in 12 hours, respectively (Figure 5c). Remarkably, the ball milling method produced perovskite in just one hour. Prolonged milling times resulted in a decrease in yield, again likely due to heat generation. These findings highlight the intricate balance required in optimizing the synthesis parameters to maximize the photocatalytic performance of DMA-modified perovskites. The study provides valuable insights into the effects of DMA cation incorporation, milling speed, and time on the structural integrity and photocatalytic efficiency of perovskites. The reproducibility of the DMA50 catalyst was performed for photocatalytic CO_2 reduction in three runs at identical experimental conditions. The results shown in Figure 5d indicate good reproducibility of the DMA50 photocatalyst.

To demonstrate that perovskites can be prepared through a simple ball milling method while maintaining water stability, the DMA50 was immersed in water for 24 hours and further investigated its photophysical properties as shown in Figure S8 (Supporting Information). First, the measurements of the XPS spectra before (Figure S8a, Supporting Information) and after (Figure S8b, Supporting Information) water treatment to confirm the oxidation state of tin in the 3d orbital. The full width at half maximum (FWHM) and binding energy showed almost no change before and after water treatment, with the two spectra nearly perfectly overlapping, indicating that Sn^{2+} was not oxidized to Sn^{4+} in the presence of water. To further confirm the ratio of Sn^{2+} to Sn^{4+} oxidation states in the perovskite, the Gaussian Function was used to fit for the Sn $3d_{5/2}$ split peak. The Sn^{2+} signal peak was positioned at 486.3 eV, while the Sn^{4+} signal peak was at 487.3 eV. According to the fitting results, the proportion of Sn^{4+} before water treatment was 7.3%. The effective reduction in Sn^{4+} generation was primarily due to the strong coordination ability of the SCN replacing iodine as the X-site anion in the perovskite. However, pseudohalogen alone were insufficient to protect the perovskite in a high-humidity environment, as evidenced by the negligible photocatalytic efficiency of DMA0 when exposed to moisture. After water treatment, the proportion of Sn^{4+} in DMA50 increased by only 4.9%, reaching 12.2%. This improvement was undoubtedly due to the addition of DMA cations, which prevented water vapor from interfering with the tin perovskite, a crucial protection in photocatalytic systems. Furthermore, XRD spectra showed that DMA50 retained its perovskite characteristics after water treatment. Similarly, the absorption spectra of DMA50 before and after water treatment showed no change in the bandgap. These findings underscore the robustness and stability of DMA50 perovskite in aqueous environments, validating the efficiency of solvent-free ball milling as an effective synthetic method. The ability of DMA cations to protect the perovskite structure from moisture-induced degradation is crucial for maintaining photocatalytic performance. This study highlights the potential for practical applications of perovskite materials in environments where moisture stability is essential.

To investigate the distinctiveness of DMA cations in the context of perovskite stability, this study also evaluated various other A-site cations (without DMA incorporating), including methylammonium (MA), ethylammonium (EA), 2-hydroxylethylammonium (HEA), guanidinium (GA), and imidazolium (IM); their corresponding chemical structures are shown in Figure S9 (Supporting Information). These cations were subjected to ball milling at 400 rpm for one hour. Unlike MA, which has a significantly smaller ionic radius than FA, the dimensions of the other tested cations are generally comparable to those of FA, and their molecular structures are predominantly linear or planar. Furthermore, the positive charge is centrally located on the nitrogen atom in these molecules, and they lack hydrophobic functional groups that could potentially confer enhanced stability. Experimental results demonstrated that upon attempting purification using deionized water, all samples readily dissolved. These findings underscore the pivotal role of both molecular structure and the presence of hydrophobic functional groups in enhancing the water stability of perovskites, thus offering crucial insights for the design of photocatalytic experiments aiming at utilizing such materials as potential candidates for photocatalytic CO_2 reduction. Moreover, in comparison to previous studies on the photocatalytic applications of tin-based perovskites (see Table S5, Supporting Information), the solvent-free ball-milled pseudohalide tin perovskites developed in this study is the first example to exhibit the remarkable ability to catalyze the reduction of CO_2 to CO without the use of sacrificial reagents. This advancement not only simplifies the reaction conditions by eliminating the need for additional chemical agents but also enhances the sustainability and practicality of the photocatalytic process. Sacrificial reagents often introduce extra costs and potential environmental hazards; therefore, their absence in our system underscores the efficiency and eco-friendliness of our perovskite materials. The ability to facilitate CO_2 reduction solely under light irradiation highlights the significant potential of these materials for practical applications in carbon capture and utilization technologies.

3. Conclusion

Tin-based perovskites are potential candidates to be applied for lead-free perovskite solar cells. However, they are sensitive to the moisture so that it is almost impossible for them to be applied in photocatalytic CO_2 reduction or H_2 evolution reaction. Herein we developed a solvent-free ball milling method to synthesize mixed-cationic pseudohalide tin perovskites for photocatalysis applications. Compared to traditional methods, ball milling allowed the preparation of perovskites at lower temperatures with a shorter reaction time, demonstrating high catalytic effectiveness and energy savings. By replacing halides with thiocyanate anions and incorporation of DMA cations together with FA cations, the study imparted significant water stability to the tin perovskite structure. The investigation into the photophysical properties of these perovskites revealed that the introduction of DMA cations resulted in a notable increase in the band gap, attributed to lattice expansion and weakened B-X bond strength. The UPS spectra analysis confirmed that varying DMA cation ratios significantly impacted the VBM levels, with an increasing DMA ratio leading to a lowered VBM level. This observation aligned with the predicted changes in the electronic structure model based on molecular orbital theory. Photocatalytic experiments demonstrated that the DMA50 perovskite ($DMA_{0.5}FA_{0.5}SnI(SCN)_2$) exhibited the highest catalytic efficiency, achieving a CO production yield of 285 μmol g^{-1} in 12 hours, outperforming the tin perovskites with other DMA ratios. The stability tests, including water immersion for 24 hours, indicated that the DMA50 perovskite maintained its structural integrity and electronic properties, with minimal oxidation of Sn^{2+} to Sn^{4+}. This confirmed the protective role of DMA cations against moisture-induced degradation. The successful application of co-cationic pseudohalide tin perovskites in photocatalytic CO_2 reduction highlights their potential in practical environmental applications. This research is the first to apply pseudohalide tin perovskites in photocatalytic experiments, effectively overcoming the issue of catalyst poisoning by moisture. By utilizing a solvent-free ball milling method, this study advanced the practice of green chemistry, minimizing the carbon footprint in experimental design. This approach not only meets modern scientific research's environmental protection requirements but also provides technological support for achieving high-standard goals of net-zero carbon emissions.

Supporting Information

Supporting Information is available from the Wiley Online Library or from the author.

Acknowledgements

The authors gratefully acknowledge the support by the National Science and Technology Council (NSTC), Taiwan (grant NSTC 112-2639-M-A49-001-ASP and NSTC 113-2639-M-A49-001-ASP) and the Center for Emergent Functional Matter Science of National Yang-Ming Chiao Tung University (NYCU) from the Featured Areas Research Center Program within the framework of the Higher Education Sprout Project by the Ministry of Education (MOE) in Taiwan.

Conflict of Interest

The authors declare no conflict of interest.

Data Availability Statement

Research data are not shared.

Keywords

ball milling, CO_2 reduction, dimethylammonium, photocatalysis, pseudohalide perovskite

Received: October 2, 2024
Revised: November 8, 2024
Published online:

[1] C. Hepburn, E. Adlen, J. Beddington, E. A. Carter, S. Fuss, N. M. Dowell, J. C. Minx, P. Smith, C. K. Williams, *Nature* **2019**, *575*, 87.

[2] H. Shen, T. Peppel, J. Strunk, Z. Sun, *Sol. RRL* **2020**, *4*, 1900546.
[3] J. Chen, T. Li, X. An, D. Fu, *Energy Fuels* **2024**, *38*, 7614.
[4] R. E. Blankenship, in *Molecular mechanisms of photosynthesis*, John Wiley & Sons, Hoboken, New Jersey **2021**.
[5] S. Ahmed, M. Irshad, W. Yoon, N. Karanwal, J. R. Sugiarto, M. K. Khan, S. K. Kim, J. Kim, *Appl. Catal. B: Environ.* **2023**, *338*, 123052.
[6] X. Duan, J. Xu, Z. Wei, J. Ma, S. Guo, S. Wang, H. Liu, S. Dou, *Adv. Mater.* **2017**, *29*, 1701784.
[7] C. D. Windle, R. N. Perutz, *Coord. Chem. Rev.* **2012**, *256*, 2562.
[8] J. Ran, M. Jaroniec, S. Z. Qiao, *Adv. Mater.* **2018**, *30*, 1704649.
[9] K. Nakata, A. Fujishima, *J. Photochem. Photobiol. C: Photochem. Rev.* **2012**, *13*, 169.
[10] L. Peng, B. Jurca, A. Garcia-Baldovi, L. Tian, G. Sastre, A. Primo, V. Parvulescu, A. Dhakshinamoorthy, H. Garcia, *Nanomater.-Basel* **2024**, *14*, 476.
[11] X. Xiang, L. Wang, J. Zhang, B. Cheng, J. Yu, W. Macyk, *Adv. Photonics Res.* **2022**, *3*, 2200065.
[12] W. Wang, L. Wang, W. Su, Y. Xing, *J. CO2 Util.* **2022**, *61*, 102056.
[13] S. D. Stranks, G. E. Eperon, G. Grancini, C. Menelaou, M. J. Alcocer, T. Leijtens, L. M. Herz, A. Petrozza, H. J. Snaith, *Science* **2013**, *342*, 341.
[14] L. Protesescu, S. Yakunin, M. I. Bodnarchuk, F. Krieg, R. Caputo, C. H. Hendon, R. X. Yang, A. Walsh, M. V. Kovalenko, *Nano Lett.* **2015**, *15*, 3692.
[15] S. Park, W. J. Chang, C. W. Lee, S. Park, H.-Y. Ahn, K. T. Nam, *Nat. Energy* **2017**, *2*, 16185.
[16] N.-N. Guo, Z.-L. Liu, Y.-F. Mu, M.-R. Zhang, Y. Yao, M. Zhang, T.-B. Lu, *Chin. Chem. Lett.* **2022**, *33*, 3039.
[17] Y. Zhao, Y. Wang, X. Liang, H. Shi, C. Wang, J. Fan, X. Hu, E. Liu, *Appl. Catal. B: Environ.* **2019**, *247*, 57.
[18] J. Schoonman, *Chem. Phys. Lett.* **2015**, *619*, 193.
[19] M. Ren, X. Qian, Y. Chen, T. Wang, Y. Zhao, *J. Hazard. Mater.* **2022**, *426*, 127848.
[20] E. Jokar, C.-H. Chien, A. Fathi, M. Rameez, Y.-H. Chang, E. W.-G. Diau, *Energy Environ. Sci.* **2018**, *11*, 2353.
[21] E. Jokar, C. H. Chien, C. M. Tsai, A. Fathi, E. W. G. Diau, *Adv. Mater.* **2019**, *31*, 1804835.
[22] A. Bard, in *Standard potentials in aqueous solution*, Routledge, Milton Park, Abingdon, Oxfordshire **2017**.
[23] M. Awais, R. L. Kirsch, V. Yeddu, M. I. Saidaminov, *ACS Mater. Lett.* **2021**, *3*, 299.
[24] M. Konstantakou, T. Stergiopoulos, *J. Mater. Chem. A* **2017**, *5*, 11518.
[25] P. Mahajan, R. Datt, W. C. Tsoi, V. Gupta, A. Tomar, S. Arya, *Coord. Chem. Rev.* **2021**, *429*, 213633.
[26] Z. Xu, M. Chen, S. F. Liu, *J. Energy Chem.* **2019**, *36*, 106.
[27] M. Rameez, E. Y. Lin, P. Raghunath, S. Narra, D. Song, M. C. Lin, C. H. Hung, E. W. Diau, *ACS Appl. Mater. Interfaces* **2020**, *12*, 21739.
[28] G. E. Eperon, K. H. Stone, L. E. Mundt, T. H. Schloemer, S. N. Habisreutinger, S. P. Dunfield, L. T. Schelhas, J. J. Berry, D. T. Moore, *ACS Energy Lett.* **2020**, *5*, 1856.
[29] L. Romani, A. Speltini, F. Ambrosio, E. Mosconi, A. Profumo, M. Marelli, S. Margadonna, A. Milella, F. Fracassi, A. Listorti, *Angew. Chem., Int. Ed.* **2021**, *60*, 3611.
[30] D. Ju, X. Zheng, J. Liu, Y. Chen, J. Zhang, B. Cao, H. Xiao, O. F. Mohammed, O. M. Bakr, X. Tao, *Angew. Chem., Int. Ed.* **2018**, *57*, 14868.
[31] Y.-F. Xu, M.-Z. Yang, B.-X. Chen, X.-D. Wang, H.-Y. Chen, D.-B. Kuang, C.-Y. Su, *J. Am. Chem. Soc.* **2017**, *139*, 5660.
[32] S. S. Bhosale, E. Jokar, Y. T. Chiang, C. H. Kuan, K. Khodakarami, Z. Hosseini, F. C. Chen, E. W.-G. Diau, *ACS Appl. Energy Mater.* **2021**, *4*, 10565.
[33] X. Li, Y. Wu, S. Zhang, B. Cai, Y. Gu, J. Song, H. Zeng, *Adv. Funct. Mater.* **2016**, *26*, 2435.
[34] X. Li, F. Cao, D. Yu, J. Chen, Z. Sun, Y. Shen, Y. Zhu, L. Wang, Y. Wei, Y. Wu, *Small* **2017**, *13*, 1603996.
[35] M. Chen, Y. Zou, L. Wu, Q. Pan, D. Yang, H. Hu, Y. Tan, Q. Zhong, Y. Xu, H. Liu, *Adv. Funct. Mater.* **2017**, *27*, 1701121.
[36] D. Chen, G. Fang, X. Chen, L. Lei, J. Zhong, Q. Mao, S. Zhou, J. Li, *J. Mater. Chem. C* **2018**, *6*, 8990.
[37] Y. Tong, E. Bladt, M. F. Aygüler, A. Manzi, K. Z. Milowska, V. A. Hintermayr, P. Docampo, S. Bals, A. S. Urban, L. Polavarapu, *Angew. Chem., Int. Ed.* **2016**, *55*, 13887.
[38] L. Rao, Y. Tang, C. Song, K. Xu, E. T. Vickers, S. Bonabi Naghadeh, X. Ding, Z. Li, J. Z. Zhang, *Chem. Mater.* **2018**, *31*, 365.
[39] D. Chen, J. Li, X. Chen, J. Chen, J. Zhong, *ACS Appl. Mater. Interfaces* **2019**, *11*, 10059.
[40] S. S. Bhosale, A. K. Kharade, E. Jokar, A. Fathi, S. M. Chang, E. W. Diau, *J. Am. Chem. Soc.* **2019**, *141*, 20434.
[41] N. Leupold, K. Schötz, S. Cacovich, I. Bauer, M. Schultz, M. Daubinger, L. Kaiser, A. Rebai, J. Rousset, A. Köhler, P. Schulz, R. Moos, F. Panzer, *ACS Appl. Mater. Interfaces* **2019**, *11*, 30259.
[42] Z. Hong, D. Tan, R. A. John, Y. K. E. Tay, Y. K. T. Ho, X. Zhao, T. C. Sum, N. Mathews, F. García, H. S. Soo, *iScience* **2019**, *16*, 312.
[43] E. Jokar, H. S. Chuang, C. H. Kuan, H. P. Wu, C. H. Hou, J. J. Shyue, E. Wei-Guang Diau, *J. Phys. Chem. Lett.* **2021**, *12*, 10106.
[44] D. Ju, X. Zheng, J. Liu, Y. Chen, J. Zhang, B. Cao, H. Xiao, O. F. Mohammed, O. M. Bakr, X. Tao, *Angew. Chem., Int. Ed.* **2018**, *57*, 14868.
[45] W. L. Tan, C. R. McNeill, *Appl. Phys. Rev.* **2022**, *9*, 021310.
[46] J. I. Langford, A. J. C. Wilson, *J. Appl. Crystallogr.* **1978**, *11*, 102.
[47] D. P. McMeekin, P. Holzhey, S. O. Fürer, S. P. Harvey, L. T. Schelhas, J. M. Ball, S. Mahesh, S. Seo, N. Hawkins, J. Lu, *Nat. Mater.* **2023**, *22*, 73.
[48] X. Liu, R. Hong, C. Tian, *J. Mater. Sci.: Mater. Electron.* **2009**, *20*, 323.
[49] G. Kieslich, S. Sun, A. K. Cheetham, *Chem. Sci.* **2015**, *6*, 3430.
[50] T. H. Chowdhury, Y. Reo, A. R. B. M. Yusoff, Y. Y. Noh, *Adv. Sci.* **2022**, *9*, 2203749.
[51] Y. Chen, Y. Sun, J. Peng, J. Tang, K. Zheng, Z. Liang, *Adv. Mater.* **2018**, *30*, 1703487.
[52] S. Ahmad, P. Fu, S. Yu, Q. Yang, X. Liu, X. Wang, X. Wang, X. Guo, C. Li, *Joule* **2019**, *3*, 794.
[53] P. Kubelka, F. Munk, *Z. Tech. Phys.* **1931**, *12*, 259.
[54] W.-J. Yin, T. Shi, Y. Yan, *Appl. Phys. Lett.* **2014**, *104*, 063903.
[55] R. Prasanna, A. Gold-Parker, T. Leijtens, B. Conings, A. Babayigit, H. G. Boyen, M. F. Toney, M. D. McGehee, *J. Am. Chem. Soc.* **2017**, *139*, 11117.
[56] J. Shamsi, A. S. Urban, M. Imran, L. De Trizio, L. Manna, *Chem. Rev.* **2019**, *119*, 3296.